

Available online at [www.sciencedirect.com](http://www.sciencedirect.com)

**jmr&t**  
Journal of Materials Research and Technology  
journal homepage: [www.elsevier.com/locate/jmrt](http://www.elsevier.com/locate/jmrt)



## Original Article

# Enhancement of electrical conductivity and corrosion resistance by gold-nickel coating of additively manufactured AlSi10Mg alloy



Timo Rautio <sup>a</sup>, Hamidreza Torbati-Sarraf <sup>b</sup>, Tarek Allam <sup>c,d</sup>,  
Antti Järvenpää <sup>a</sup>, Atef Hamada <sup>a,\*</sup>

<sup>a</sup> Kerttu Saalasti Institute, University of Oulu, Pajatie 5, 85500, Nivala, Finland

<sup>b</sup> School of Materials Engineering, Purdue University, West Lafayette, IN, 47907, USA

<sup>c</sup> Steel Institute, RWTH Aachen University, Intzestraße 1, 52072, Aachen, Germany

<sup>d</sup> Department of Metallurgical and Materials Engineering, Suez University, 43528, Suez, Egypt

## ARTICLE INFO

## Article history:

Received 6 October 2021

Accepted 5 January 2022

Available online 12 January 2022

## Keywords:

Gold-nickel coating

AlSi10Mg alloy

Additive manufacturing

Electrical resistivity

Corrosion resistance

## ABSTRACT

Gold-nickel coatings (Au–Ni) were applied by electrodeposition (ED) and electroless deposition (ELD) on additively manufactured (AM) AlSi10Mg alloy to improve the electrical conductivity and electrochemical behavior. Characterization of the Au–Ni coatings was performed by a scanning electron microscope equipped with energy dispersive X-ray spectroscopy (EDS) and x-ray diffraction to study the tiny features. The surface indentation hardness of the coated alloy was evaluated to study the coating strength. The electrochemical behavior of the as-built part and its counterpart, Au–Ni coated surfaces, were evaluated by conducting potentiodynamic polarization (PDP) and electrochemical impedance spectroscopy (EIS) in a 3.5% NaCl solution.

The results revealed that the Au–Ni coatings with layers thickness of ~2 and 10 μm, respectively, could overcome the surface critical defects, i.e., pores and flaws. The surface hardness of the coated AM alloy has significantly increased six times due to the hard Ni layer. The electrochemical measurements showed a significant decrease in the anodic dissolution rate and increase in pitting corrosion resistance for the Au–Ni coated surfaces compared to the bare AM AlSi10Mg alloy with the as-built and polished surface condition in chloride solution. This was attributed to the stability of the Au–Ni coatings against the anodic overpotential. Moreover, it was observed that the Au–Ni coatings reduce the electrical resistance of the studied AM alloy by 40%. Consequently, the surface electrical conductivity property of the AM AlSi10Mg alloy was enhanced by both Au–Ni coating procedures.

© 2022 The Author(s). Published by Elsevier B.V. This is an open access article under the CC BY-NC-ND license (<http://creativecommons.org/licenses/by-nc-nd/4.0/>).

\* Corresponding author.

E-mail address: [atef.hamadasaleh@oulu.fi](mailto:atef.hamadasaleh@oulu.fi) (A. Hamada).

<https://doi.org/10.1016/j.jmrt.2022.01.022>

2238-7854/© 2022 The Author(s). Published by Elsevier B.V. This is an open access article under the CC BY-NC-ND license (<http://creativecommons.org/licenses/by-nc-nd/4.0/>).

## 1. Introduction

Additive manufacturing (AM) is currently challenging traditional manufacturing technologies in a wide spectrum of industry areas, and it has been adopted by several industries such as automotive [1,2], biomedical [3], dentistry [4] and aerospace [5,6]. The ability to design complex parts with great design freedom at low cost, reduction in weight and material costs and small series production with low tool costs are among the most important benefits compared to the traditional manufacturing methods that have pushed the industrial adoption of AM. While its advantages are obvious, there are still challenges that need to be addressed for the even wider deployment of AM. Relatively high surface roughness [7,8], peculiar inner defect distribution [9,10] with surface defects such as voids and micro-cracks [11] are some of the key issues that should be considered.

Laser powder bed fusion (L-PBF) is currently the most widely deployed technique in the field of metal AM. The metals that have been successfully produced by AM are including titanium and its alloys [12,13], nickel-based alloys [14,15], iron-based alloys [16,17], and aluminum and its alloys [18,19]. The ability to use high power and fast scanning speed with applying high layer thickness has made aluminum alloy, particularly AlSi10Mg, one of the most effective materials for L-PBF manufacturing. It possesses good machinability, high strength, and durability with high corrosion resistance in addition to good thermal properties and low weight enabling a wide range of applications.

A significant number of studies on AM AlSi10Mg focused on the mechanical properties [20–22], fatigue properties [23–25], optimizing process parameters [26,27], and microstructure evolution [28–30]. The electrical properties of AlSi10Mg attract increasing attention as a cost-effective alternative to the more expensive copper [31]. However, the oxidation of aluminum alloys generally limits their implementation in electrical applications, as the presence of an oxide layer on the surface reduces the conductivity. One of the well-known techniques to mitigate the oxidation-induced low electrical conductivity of aluminum alloys is coating with a more noble metal such as silver or gold. It is worth mentioning that the coating with such noble metals enhances the corrosion resistance as well. The authors' previous work showed that silver-copper coatings can be utilized to enhance the electrical conductivity and to improve the corrosion resistance of AM AlSi10Mg [32]. In high-end applications where the corrosion properties are of the highest priority and the additional cost can be justified, gold coatings are commonly applied. Ingberg et al. [33] studied electroless gold coating in terms of optical microscopy, XRD analysis, surface roughness, and SEM imaging. Ashkenazi et al. [34] investigated the electroless deposition of Ag, Au, and Au–Ag alloys on L-PBF AlSi10Mg. In a following work, Inberg et al. [35] focused only on the Au–Ag electroless plating of the same material.

Corrosion properties of AM AlSi10Mg with as-built and coated surface have been rarely reported. Pezzato et al. referred to an increase in corrosion resistance by applying plasma electrolytic oxidation on the AlSi10Mg samples manufactured at different porosity levels [36]. Rafieezad et al.

reported a success on applying friction stir processing on the AlSi10Mg to improve the corrosion properties [37]. In the authors' previous work, silver-copper coatings were utilized to enhance the corrosion resistance and to increase the electrical conductivity of AlSi10Mg manufactured by L-PBF compared to the as-built state. It was demonstrated that in spite of the significant improvement in the corrosion resistance of the silver-copper coated specimens, their surfaces were not free from corrosion. That is why we applied a newly developed gold-nickel coating aiming at further enhancement of corrosion resistance of AlSi10Mg manufactured by L-PBF. In the current study, the copper coating is replaced by nickel to avoid the interdiffusion of gold and copper that limits the usability of gold-copper coatings in high-temperature environments and where a long lifetime is desired [38]. An additional advantage of using nickel coating is that both gold and nickel layers can be deposited with smaller thicknesses than their silver and copper counterparts, which is beneficial in terms of cost and weight reduction of the final parts.

The present work aims to evaluate the utilization of gold-nickel (Au–Ni) layers applied on AM AlSi10Mg surface, to show its effect on enhancing the electrical conductivity and corrosion performance in a chloride solution. The Au–Ni coatings of AM AlSi10Mg have been processed by two different techniques, namely, electroless deposition (ELD) and electrodeposition (ED) coating.

## 2. Material and methods

### 2.1. Material and L-PBF manufacturing

An SLM 280 HL machine based on the L-PBF technique was utilized to manufacture the samples required in this work. Carpenter Additive of Carpenter Technology Corporation (UK) supplied the spherically shaped AlSi10Mg powder with the chemical composition as shown in Table 1. The powder particle size range was 20–63  $\mu\text{m}$  with the highest volume fraction of 37  $\mu\text{m}$  diameter. Focusing on the general usability of the coating process, the standard parameters as delivered by the machine supplier were applied for L-PBF manufacturing of the required samples. The relevant parameters were as follows: laser power ( $P$ ) of 370 W, laser speed ( $v$ ) of 1335 mm/s, hatch spacing ( $h$ ) of 0.17 mm, layer thickness ( $t$ ) of 30  $\mu\text{m}$  and laser spot diameter of 0.15 mm. Consequently, the applied energy density of 54.3 J/mm<sup>3</sup> was calculated from Eq. (1)

$$E = \frac{P}{v \cdot h \cdot t} \quad (1)$$

The printing platform was preheated to 100 °C and held constant during the printing. The process was carried out under argon atmosphere at a pressure of 12 mbar with a gas

**Table 1 – Chemical composition in wt.% of the AlSi10Mg powder used for L-PBF processing.**

Al	Si	Mg	Fe	Mn	Cu	Zn	Ti	Ni
Bal.	9–11	0.2–0.45	0.55	0.45	0.05	0.1	0.15	0.05

**Table 2 – Process flow of the gold-nickel plating for electroless and electrodeposited coatings with the used bath compositions and process conditions.**

Process	Bath composition	Conditions	Concentration, g/L
(a) Electrolytic cleaning	Alkaline solution	Temp.: 35 °C; time: 12 min, $I = 4 \text{ A/dm}^2$	6
(b) Rinse	Tap water		
(c) Activation	HNO <sub>3</sub>	Temp.: RT; time: 2 min	50 vol-%
(d) Rinse	Tap water		
(e) Zincation	HSO Zincate Pickle II	Temp.: RT; time: 1 min	75
(f) Rinse	DI water		
(g) Electroless deposition of nickel (ELD)	- Nickel sulfate, Conc. Ni <sup>2+</sup> - Sodium hypophosphite,	pH: 5; temp.: 89 °C, time: 30 min	6 200
Electrodeposition of nickel (ED)	OR - Nickel sulfate, Conc. Ni <sup>2+</sup> - Nickel chloride, Conc. Cl <sup>-</sup> -Boric acid	pH: 4; temp.: = 59 °C, time: 15 min, $I = 3 \text{ A/dm}^2$	70 18 45
(h) Rinse	DI water		
(i) Gold plating	Conc. Au <sup>+</sup>	pH: 4.2; temp.: RT; time: 25 min square wave pulse, $I_A = 2 \text{ A/dm}^2$	4

flow rate of 7.5 m/s. Plates in the size of  $30 \times 150 \times 3 \text{ mm}^3$  were positioned in 25° angle towards the gas flow on the platform of  $280 \times 280 \text{ mm}^2$ . The building direction of the samples was horizontal (0°).

The as-built AM AlSi10Mg alloy was undergone a stress relief heat treatment (T5-HT) at 300 °C for 2 h in a muffle furnace under an argon atmosphere.

## 2.2. Gold-nickel coating

Multilayer coatings from gold-nickel (Au–Ni) coatings were applied on AM AlSi10Mg plates with dimensions of  $30 \times 150 \times 3 \text{ mm}^3$ . The internal Ni layer was synthesized by

applying two different deposition techniques, ED and ELD. However, the top surface Au layer was processed by one deposition technique, ED.

The Au–Ni coatings were conducted in Eforit Oy, Sipoo, Finland. The processes of both deposition techniques include multiple steps and are collected in Table 2. The plates first underwent a thorough cleaning by electrolytic cleaning for 12 min at a current density of  $4 \text{ A/dm}^2$  in an alkaline solution followed by rinsing in tap water. The cleaned plates were then activated in nitric acid for 2 min at room temperature and rinsed again in tap water. The last preparing process prior to the actual Au–Ni was the development of a base layer by zincation process. After a rinse in deionized water

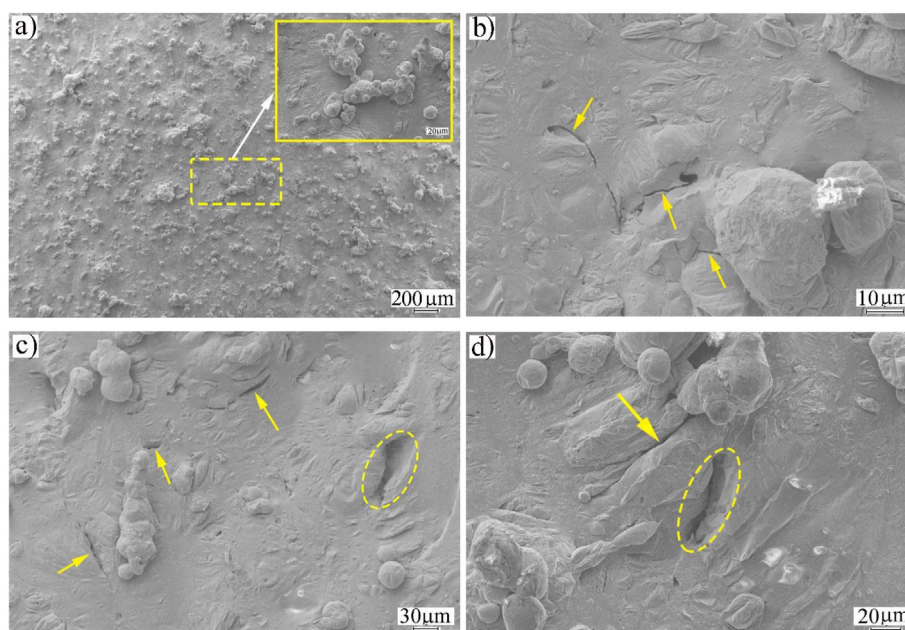


**Fig. 1 – SEM micrographs of the surface features of the as-built L-PBF manufactured AlSi10Mg alloy. a) reveals the high surface roughness due to incompletely melted powder particles (the inset in the upper right corner), b), c) and d) show the presence of pores and cracks with different forms.**

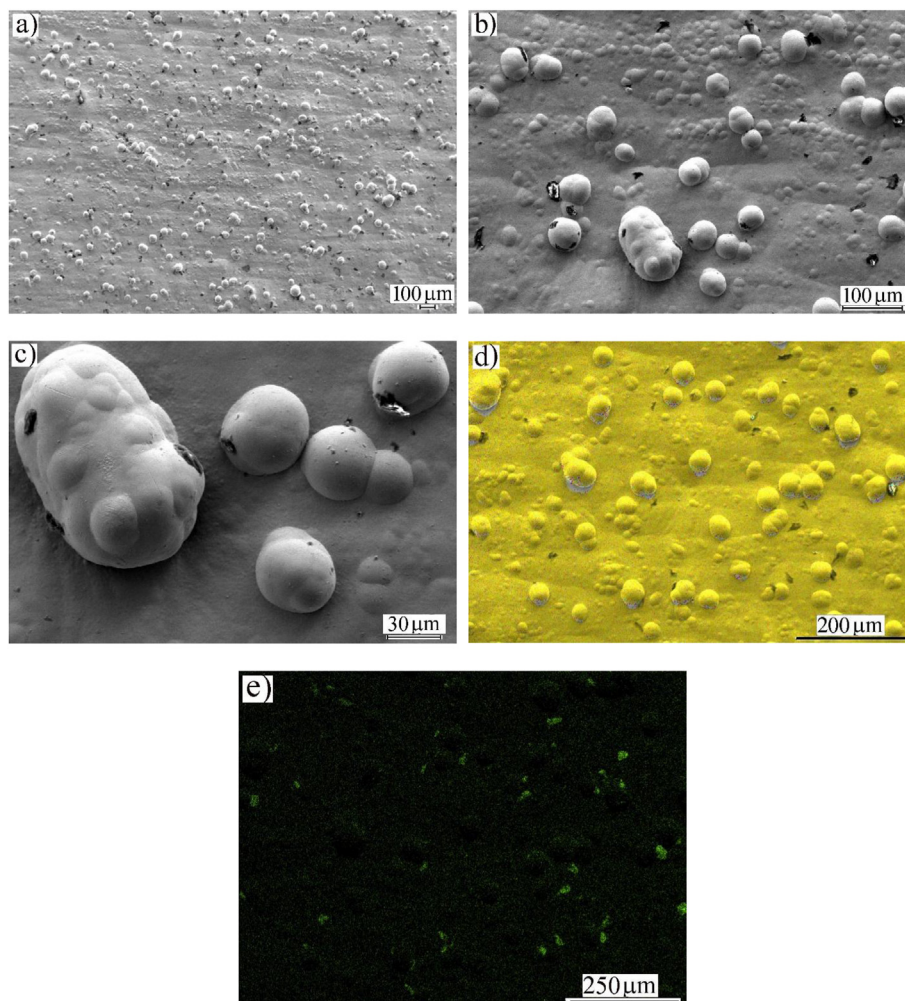


**Fig. 2** – SEM images of the surface appearance of AM AlSi10Mg alloy after Au–Ni coating via electrodeposition technique. a) an overview of the surface features, b) and c) high magnification micrographs and d) EDS map showing the presence of Au, P and C in gold, red and black colors, respectively. e) EDS distribution elemental map of C.

(DI), the Ni layer was deposited on two sets of samples using ELD as well as ED techniques. The ELD Ni coating was conducted in 30 min while electroplating could be finished in 15 min at  $3\text{A}/\text{dm}^2$ . The temperature during the ELD Ni layer was maintained at  $89\text{ }^\circ\text{C}$ , which is higher than that applied during the ED process of  $59\text{ }^\circ\text{C}$ . A final rinse in DI water was applied before proceeding with the Au coating. Square wave pulse at an average current density of  $2\text{ A}/\text{dm}^2$  was utilized during the gold electrodeposition process to manage the Au shell coating.

### 2.3. Characterization

#### 2.3.1. Surface features

The micro- and surface features of the as-built AlSi10Mg alloy and the corresponding Au–Ni coated alloy were observed by using a field-emission gun scanning electron microscope (FEG-SEM) (Carl Zeiss Ultra plus). Secondary electron micrographs were captured at an operating voltage of 5 kV. Also X-ray diffraction (XRD) data acquisition was carried out for

phase analysis in a Rigaku SmartLab XRD diffractometer with Co- $K_\alpha$  radiation.

#### 2.3.2. Indentation hardness

The mechanical response of the bare AM alloy and the Au–Ni layers in terms of their indentation hardness was evaluated by microindentation hardness measurements using a CSM MHT-Z-AE microhardness tester (CSM Instruments SA of Anton Paar GmbH, Peseux, Switzerland). The areas were indented with a Vicker's indenter using a modest maximum load of 0.2 N to measure the thin Au shell layer. Subsequently, the samples were gently polished to remove the Au layer and the hardness of the Ni coating was measured. An approach indentation rate of  $200\text{ }\mu\text{m}/\text{min}$  was used to make contact to the measured surface followed by the hardness test performed by ramping up the load at a loading rate of  $0.4\text{ N}/\text{min}$  to the maximum load of 0.2 N. Unloading was performed at the same rate after a 10 s hold time at the maximum force. The Oliver-Pharr method was applied to define the material properties from the measured data.

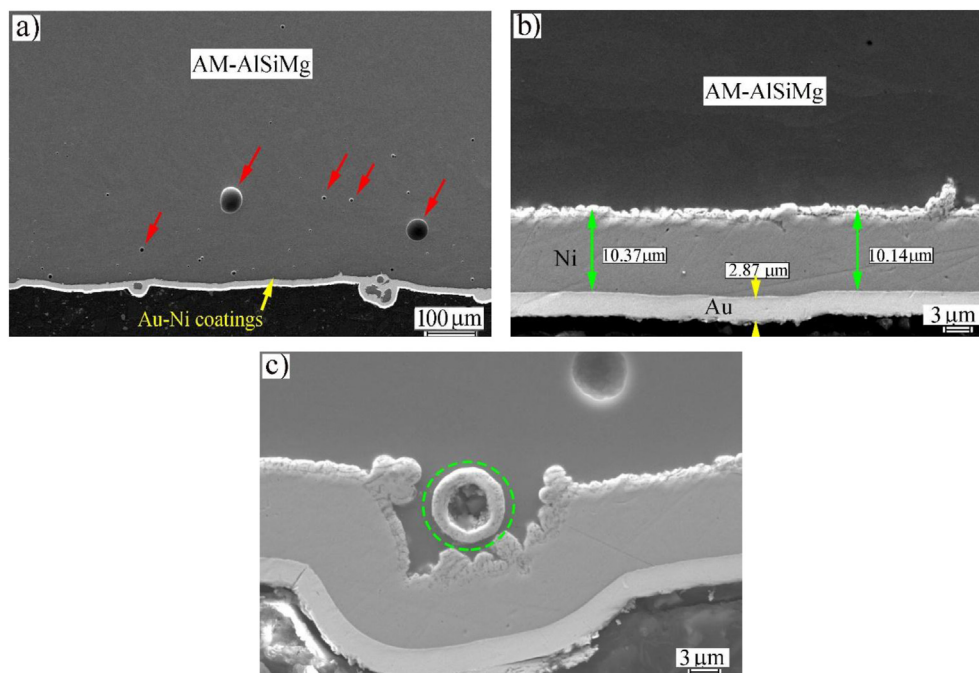


**Fig. 3 – Cross section view of the electrodeposited Au–Ni coating: a) a general view of the cross section showing the presence of internal pores in the AM structure, b) a closer view of the coating to display the thickness of Au and Ni layers, and c) a magnified view of a subsurface defect impregnated and healed by the applied Au–Ni coating (encircled in green).**

### 2.3.3. Electrical conductivity

Electrical conductivity of the LBPF manufactured AlSi10Mg after the stress relief HT was measured and repeated after the subsequent plating by ELD or ED of Au–Ni layers. Measurements were conducted using four-point collinear probes with a GW Instek 4-wire digital micro-ohmmeter (GOM-805) using the same setup as previously in [32]. For the measurements, plates with dimensions of 50 mm in length and 8 mm in width were cut from both sets with a wire EDM (Electrical Discharge Machining). In addition, the contact points at the ends of all samples were equalized by cutting shallow notches with the wire EDM.

### 2.3.4. Electrochemical tests

A 3.5wt.% NaCl solution prepared by deionized water and analytical grade of NaCl was used for corrosion analysis. All electrochemical measurements were performed by an Autolab VersaSTAT 3 using the conventional three-electrode configuration consisting of a saturated calomel electrode (SCE) and a graphite electrode as a reference and a counter electrode, respectively. The prepared surface of the examined samples served as the working electrode.

After exposing the samples in the solution for 24 h at the free potential, Electrochemical Impedance Spectroscopy (EIS) measurement was carried out at an open circuit potential (OCP) by applying a 10 mV sinusoidal perturbation potential within the range of 100 kHz to 10 mHz. The results were fitted to physically meaningful circuits using Zview software and goodness of fitted were checked using  $\chi^2$  approach.

It should be noted that during the 24 h exposure, the OCP was monitored to ensure that all the samples are in stabilized

condition for electrochemical measurements. The potentiodynamic polarization was also conducted on the examining surfaces exposed in the solution for 24 h, from  $-0.2$  V vs. OCP to  $0.2$  V vs. SCE with a scan rate of  $0.5$  mV s $^{-1}$ . The surface morphology of the bare AM material and the Au–Ni coated AM material after corrosion testing was observed by a laser scanning confocal microscope (Model: KEYENCE/VK-X100).

## 3. Results & discussion

### 3.1. Surface features of the as-built state

The AM parts in the as-built state usually exhibit a series of processing-related surface defects. Fig. 1 shows the typical surface features of the L-PBF manufactured AlSi10Mg alloy in the as-built state. It is clear from Fig. 1(a) that the surface is rough due to the incompletely melted powder particles as indicated in the upper right corner inset of Fig. 1(a). This inset clearly reveals the presence of single or accumulations of powder particles that are still adherent to the surface. The observed high surface roughness is a common feature of the AM parts, and it reaches values that are several times higher than those of machined parts [39]. The main causes of such high surface roughness of AM parts are attributed to the formation of satellites and the presence of balls due to balling phenomenon [40]. In addition to the high surface roughness, several pores and surface cracks are observed on the surface of the as-built state. These pores and cracks are of different configurations and orientations with sizes of a few tens of microns as shown in Fig. 1(b-c). The formation of small pores

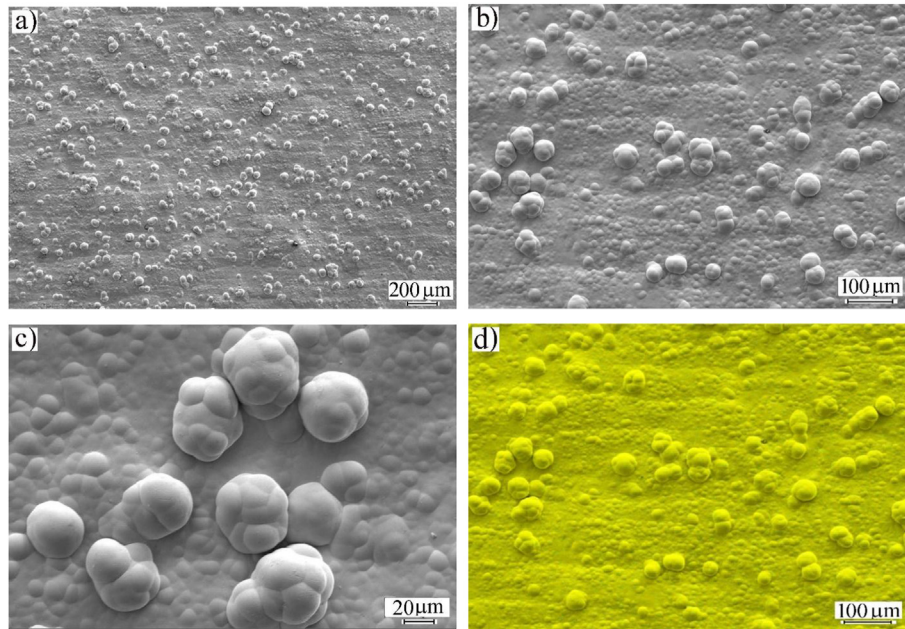


**Fig. 4** – SEM images of the surface appearance of AM AlSi10Mg alloy after Au–Ni coating via electroless deposition technique. a) an overview, b) and c) magnified SEM image of the surface features, and d) EDS elemental map indicating the presence of only Au (in gold color).

is usually ascribed to the presence of moisture on the particles of starting powder [41], while the formation of cracks is related to the high attainable cooling rates during L-PBF processing [42].

The surface features and the cross-section of the L-PBF manufactured AlSi10Mg alloy after applying the Au–Ni coating using both the ED and ELD techniques were

investigated. Fig. 2 displays the surface appearance after applying Au–Ni coating using the electrodeposition route. Obviously, the surface roughness is still high as it can be noticed from the presence of particles of various sizes as displayed in Fig. 2(a). It is demonstrated that the roughness of the Au-coated specimens decreases as the thickness of the deposited gold layer increases [33], which should be

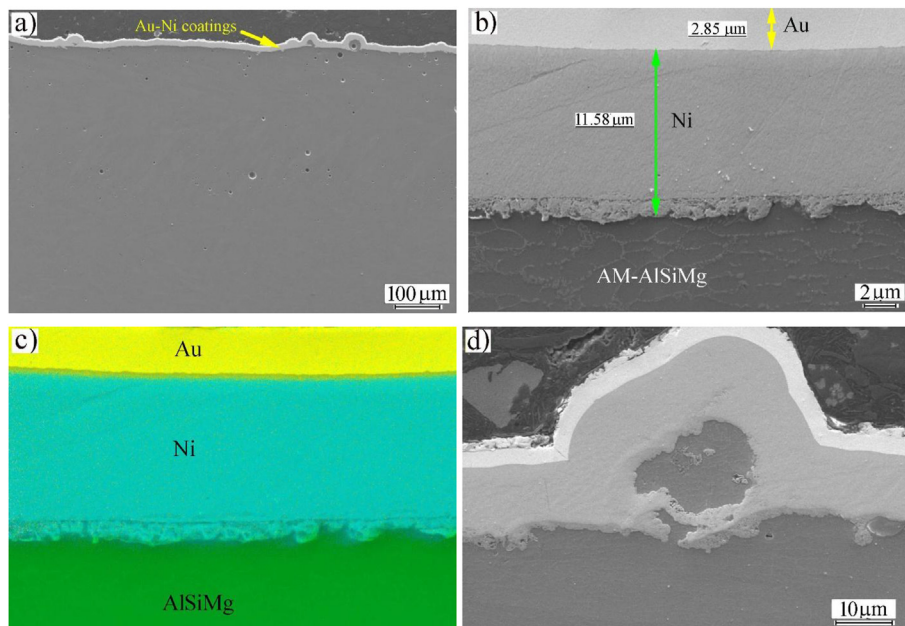


**Fig. 5** – Cross section view of the electroless deposited Au–Ni coating. a) an overview, b) a magnified SEM image of the coating showing the different thicknesses of the layers, c) EDS map through the cross section, and d) a magnified view of the subsurface defect that was sealed with the applied Au–Ni coating.

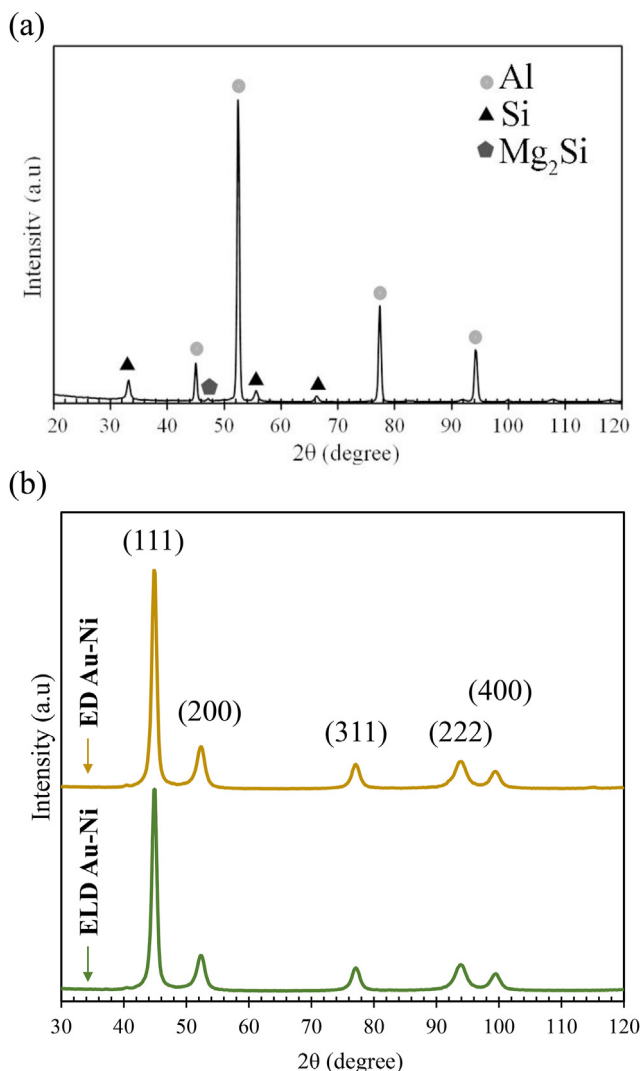


**Fig. 6 – X-ray diffraction patterns of (a) as-built and (b) electroless and electrodeposited Au–Ni coated surfaces of AM AlSi10Mg alloy.**

associated with high coating costs. A closer view of these particles (represented in Fig. 2(b and c) reveals the presence of agglomerated droplets in the size range of 30–120  $\mu\text{m}$  on the top of the coating layer. The EDS elemental map of a representative area of the surface indicates that the outer layer of the coating is consisting of Au (yellow color) and a very small fraction of P (tiny red dots) as shown in Fig. 2(d). Furthermore, the agglomerated droplets are Au-droplets which significantly contribute to the apparent high surface roughness of the coating. The small detected black spots are characterized by EDS and found to be graphite, as shown in Fig. 2(e). It is worth mentioning here that the pores and cracks are completely sealed and filled, which reflects the enhancements of surface properties and the reduction of AM processing-related defects through the applied Au–Ni coating.

Fig. 3 represents a cross-section view of the L-PBF manufactured AlSi10Mg alloy coated with Au–Ni via electrodeposition route. The general view of the cross-section, shown in Fig. 3(a), represents a couple of distinct features. The bare AM-

AlSi10Mg is still containing obvious internal pores of both relatively small and large sizes as indicated by red arrows Fig. 3(a). The observed spherical pores are denoted as metallurgical pores and their sizes can reach a few microns [43], and they formed due to the moisture or entrapped hydrogen on the surface of the particles and during processing [41]. The thickness of the Au–Ni coating is almost homogenous over the whole sample, and at higher magnification (Fig. 3(b)) both Au- and Ni-layers appear uniform with a thickness of approximately 3 and 10  $\mu\text{m}$ , respectively. Surprisingly, the Ni-layer penetrates in the open subsurface holes as can be inferred from the places where Ni-layer is surrounding isolated regions of base alloy (green circles Fig. 3(a)). A high magnification micrograph for the penetration of Ni-layer into the open subsurface holes is shown in Fig. 3(c), which demonstrates the importance of the applied coating in healing the surface as well as the opened and deep subsurface cracks and holes.

Likewise, the surface features and the cross-section of the L-PBF manufactured AlSi10Mg alloy coated with Au–Ni coating via electroless deposition route are represented in Fig. 4 and Fig. 5, respectively. Similar to the electrodeposition route, the surface roughness of Au–Ni coating deposited via the electroless deposition route is still obviously high due to the agglomerated Au-droplets as displayed in Fig. 4(a). The agglomeration of gold particles was reported before during gold plating of silica nanoparticles used in composite solders used in electronic devices [44]. The sizes of agglomerated Au-droplets within the range of 30–80  $\mu\text{m}$  are relatively smaller than those observed for the electrodeposited Au–Ni coating. A closer view of the agglomerated Au-droplets is shown in Fig. 4(b) and c. In contrary to electrodeposited Au–Ni coating, the electroless deposited one does not show the presence of P as it revealed from the EDS elemental map represented in Fig. 4(d). Furthermore, the black spots do not appear in the EDS distribution map of C, Fig. 4(e).

The general cross-section view of the electroless deposited Au–Ni coating represented in Fig. 5(a) reveals comparable features to those which are observed in the case of electrodeposited coating. The Au- and Ni layers are uniform over the whole surface with thicknesses of around 3 and 10  $\mu\text{m}$ , respectively (Fig. 5 b and c). The ability of Ni-layer to penetrate and to heal the subsurface opened holes is also observed in the case of electroless deposited coating as shown in Fig. 5(d).

X-ray diffraction patterns obtained from the surface of the as-built sample as well as Au–Ni-coated surfaces are represented in Fig. 6. The presence of the cubic Si phase and Mg<sub>2</sub>Si compound can be seen in the matrix of AlSi10Mg as-built sample, as shown in Fig. 6(a). Furthermore, XRD phase analysis confirmed the existence of Mg<sub>2</sub>Si precipitates at an angle (2 $\theta$ ) of 47.2° according to the JCPDS pattern of 00-001-1192.

XRD patterns for Au–Ni-coated surfaces reveal that both processed coatings have face center cubic (FCC) crystallographic structures, as shown in Fig. 6(b). Despite the same identified crystallographic structures for the coating developed by electro and electroless deposition, slight changes in the relative intensity of the corresponding (111) diffraction peaks can be observed. These changes were evaluated by relative texture coefficient (RTC) [46] as shown in Fig. 7. It is observed that RTC<sub>(111)</sub> for ED Au–Ni coated sample has a

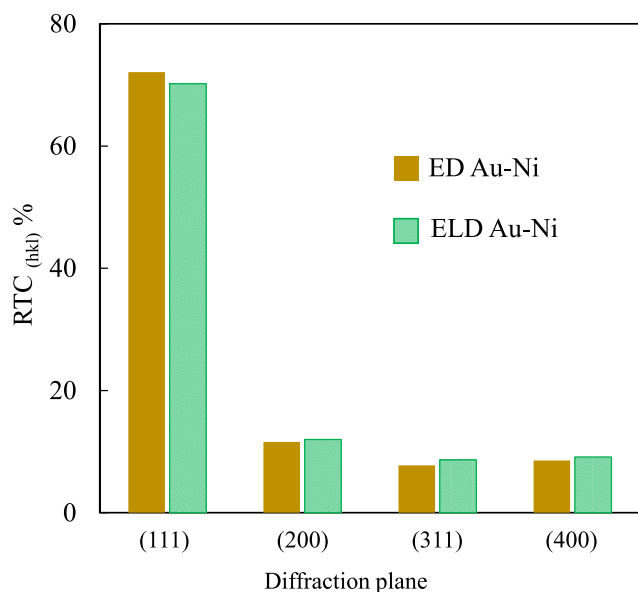


**Fig. 7 – Relative texture coefficient (RTC) values of (111), (200), (311) and (400) diffraction planes on electroless and electrodeposited Au–Ni coated surfaces of AlSi10Mg AM alloy.**

higher value than that calculated for the ELD Au–Ni coated sample between all the diffraction planes. This indicates that the majority of the grains during electrodeposition Au–Ni coating are oriented with their (111) plane, which is parallel to the surface of the deposition.

### 3.2. Electrical conductivity

Electrical resistivity (ER) of both the ED and ELD Au–Ni coated samples were measured and compared with that of the as-built surface of AM AlSi10Mg alloy. Fig. 8 illustrates the measured ER of the specimen in the as-built state and the Au–Ni coated specimens by the ED and ELD techniques. As a reference for the ER values of L-PBF manufactured AlSi10Mg in

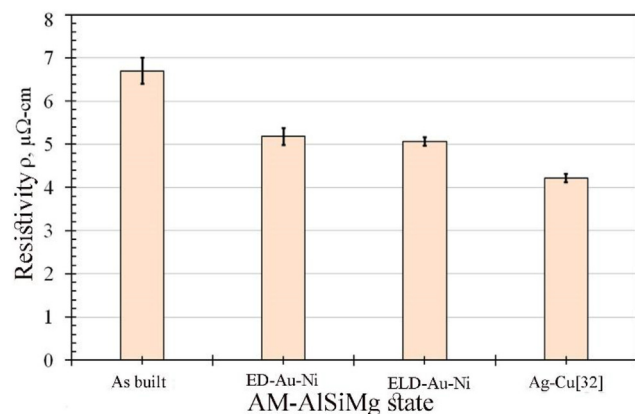


**Fig. 8 – Electrical resistivity of the bare AM AlSi10Mg and the corresponding Au–Ni coated material. For comparison, resistivity of Ag–Cu coated AM AlSi10Mg adopted from [32].**

the coated state, the ER measurements of Ag–Cu coating from our previous work [32], which was carried out with the same device and at the same testing conditions, are included in Fig. 8. Generally, it is obvious that the surface coating either with Au–Ni layers or with Ag–Cu layers has a significant improvement on the electrical conductivity of the studied AM AlSi10Mg alloy. However, the achieved improvement in the electrical conductivity of AM AlSi10Mg alloy by Ag–Cu coating is higher than that reached by Au–Ni coating using both ED and ELD techniques. This is mainly attributed to two reasons. First, the higher layer thickness of the Ag and -Cu layers, which were 4 and 35  $\mu\text{m}$ , respectively, while the thickness of Au and Ni layers in the current study is considerably lower, 2 and 10  $\mu\text{m}$ , respectively. Second, is the higher electrical conductivity of the Cu layer in Ag–Cu coating than its counterpart Ni layer in Au–Ni coating.

Based on the represented results in Fig. 8, the as-built state shows the highest ER value of 6.7  $\mu\Omega\text{-cm}$ . It is observed that the Au–Ni coating by ED technique enhances the electrical properties, as the corresponding ER value decreases to 5.18  $\mu\Omega\text{-cm}$ . In comparison to the Au–Ni coating developed by the ED technique, the Au–Ni coating using the ELD technique further decreases the ER value to 5.06  $\mu\Omega\text{-cm}$ . This emphasizes that the ELD technique is more advantageous than ED one in terms of enhancing the electrical conductivity of AM AlSi10Mg by Au–Ni coatings. Most probably, the presence of the P in the Au layer captured by EDS in Fig. 2(d) is responsible for the increase in ER value of Au–Ni coating by ED. It was demonstrated that the presence of P traces increases the ER of Al–Si alloys [45].

### 3.3. Indentation hardness

The mechanical response of the surface of L-PBF manufactured AlSi10Mg with the subsequent Au–Ni coating by two different deposition techniques was investigated by measuring the microhardness of each layer. The microhardness of the AM AlSi10Mg base material is compared to that of Au and Ni layers in the coated state developed by both ED and ELD techniques.

The resulting load-penetration depth curves measured after applying a load of 0.2 N are represented in Fig. 9(a) and the corresponding microhardness values are collected in Fig. 9(b). As expected, the results show that different material layers can be distinguished from their penetration depths and microhardness levels. The base material AM AlSi10Mg in HT condition shows the deepest penetration depth at 2.2  $\mu\text{m}$  and is hence the softest material on the specimen and has also the lowest hardening rate as can be seen from the slop of its load-penetration curve. The corresponding microhardness value is defined at 1.3 GPa. The microhardness values of the gold layer deposited by ED and ELD techniques are very close to each other, but the penetration depth on the ELD coated AM alloy is slightly lower at 1.2  $\mu\text{m}$  compared to 1.4  $\mu\text{m}$  of the ED coated AM alloy. The part of Au–Ni coated AlSi10Mg that has the highest microhardness value is the core layer Ni, which shows also the highest hardening behavior as can be seen from the corresponding load-penetration curves of both ELD and ED coated AM samples. The results show nearly identical hardness of Ni layer for the two techniques, with a penetration

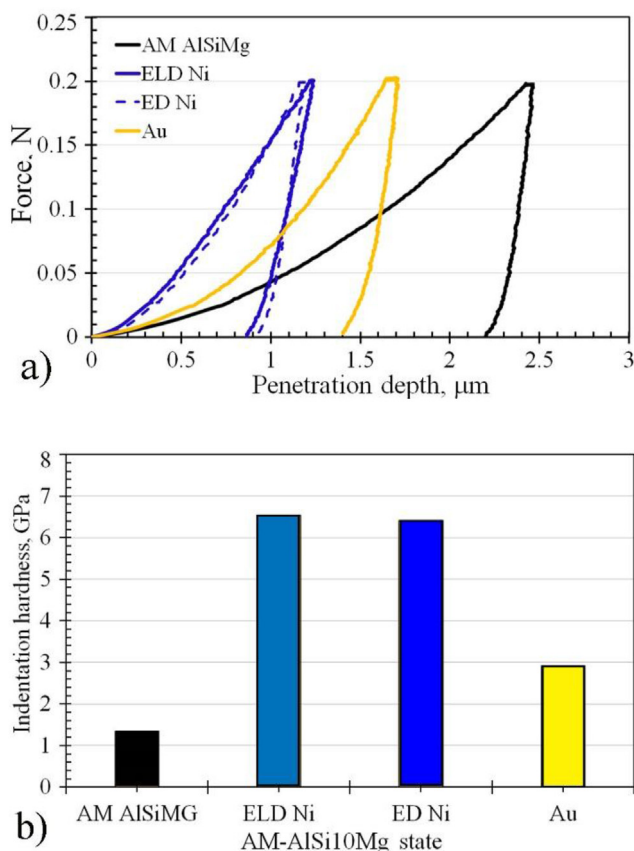


**Fig. 9 – Mechanical response of the different layers of Au–Ni coating as well as the base AM AlSi10Mg alloy. a) Load-penetration depth curves and b) the corresponding values of the indentation hardness.**

depth of around 0.9 μm that corresponds to microhardness of approximately 6.4 GPa.

### 3.4. Electrochemical behavior

Potentiodynamic polarization curves of as-built and coated samples tested in 3.5 wt.% NaCl solution are shown in Fig. 10. In this study, in order to compare the corrosion performance of the as-built surface with the bulk of the AM part, electrochemical measurements were also conducted on a freshly mirror polished surface of AM sample. The extracted corrosion parameters, such as corrosion potential ( $E_{\text{corr}}$ ), corrosion current density ( $j_{\text{corr}}$ ), anodic and cathodic Tafel slopes ( $\beta_a$  and  $\beta_b$ ) from the polarization curves, are listed in Table 3. It is noted that, due to the surface roughness, localized electrochemical reactions over the surface, and the nature of the Tafel extrapolation, the extracted numbers reveal the approximation of overall reaction on the entire surface of examined samples. Besides, as different materials with different compositions were subjected to the electrochemical tests, corrosion current density values cannot be directly interpreted as weight or thickness loss comparison.

Au–Ni coated surfaces revealed relatively nobler  $E_{\text{corr}}$  compared to as-built AM AlSi10Mg surface. However, it should

be noted that the corrosion phenomena involve a series of cathodic and anodic processes, and hence,  $E_{\text{corr}}$  is a measure of all electrochemical reactions taking place on the surface and it is not a property of a material. In near-neutral pH environments, Al is known as a corrosion-resistant metal because a protective aluminum oxide film naturally forms on its surface. However, in the case of Al alloys, this film is prone to lose its stability due to localized attack of halogen ions such as chloride and formation of galvanic couples between Al-matrix and constituent particles facing the surface [37,47,48]. In this study, one of the purposes of applying Au–Ni plating on the surface of the AM AlSi10Mg alloy was to prevent corrosion since Au is one of the noblest metals in corrosive environments. Surprisingly, greater values of  $j_{\text{corr}}$  were observed for Au–Ni coated compared to the as-built and polished AM AlSi10Mg surface. This might misleadingly imply corrosion occurs at higher rates on Au–Ni coated surfaces at OCP compared to AM AlSi10Mg alloy. However, such interpretation can be accountable for active metals but not for a noble metal such as Au or Pt which does not get oxidized in similar examining solutions [49]. Au is one of the greatest catalyst candidates for fuel cell application to enhance hydrogen evaluation reactions [50]. Hence, the dominant cathodic and anodic reaction at the surface of Au–Ni coated surface at  $E_{\text{corr}}$  can be written in Eqs. (2) and (3), respectively:



While the dominant cathodic and anodic reactions occurring on the surface of Al alloy in aerated neutral aqueous solutions are the reductions of oxygen and oxidation of Al followed by formation and precipitation of hydroxide ions on the corroding surface of Al, as written in Eqs. (4)–(6) [37,51]:



Therefore, increases in  $j_{\text{corr}}$  for the Au–Ni coated surfaces as against the Al surface, just points to the superior catalytic behavior of the coated surfaces to hydrogen evolution. Besides, comparing the polarization curve of the as-built surface with the polished condition, one can see that the higher polarization resistance of the as-built surface at the corrosion potential originates from the naturally air-formed oxide film on this surface which formed during the exposure of freshly AM processed to the air. The drastic increase of current densities at higher anodic overpotentials ( $E_{\text{pit.}} = 0.71 \text{ V vs. SCE}$  shown in Fig. 10) reveals that this film does not provide sufficient protection in anodic overpotential or long-term exposures. From the polarization curve and Tafel slope values of the polished surface, it is clear that once this protective film was removed by polishing, cathodic reaction ( $\beta_a < \beta_c$ ) controlled the corrosion reaction at corrosion potential and the current densities jumped off as soon as the anodic overpotential increased. Note that as the

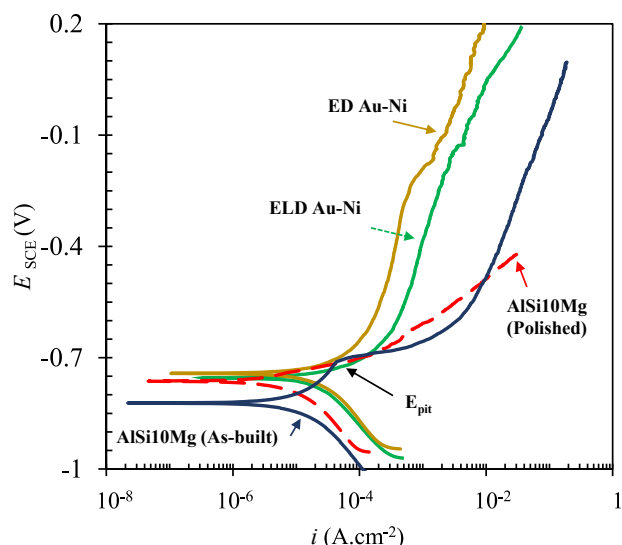


**Fig. 10** – Potentiodynamic polarization results of the AM AlSi10Mg alloy with as-built, polished and Au-Ni coated surface condition exposed in 3.5 wt.% NaCl solution for 24 h at OCP.

electrochemical equipment automatically stops the polarization measurements once the current overloads, the as-built and polished surfaces were not anodically polarized up to 0.2 V vs. SCE.

In the case of Au–Ni coated samples, greater values of  $\beta_c$  compared to  $\beta_a$  imply the cathodic reaction is the rate-determining step of electrochemical reactions in the examining solution; while for the as-built sample, both cathodic and anodic reactions have almost equal contribution in corrosion process of surface. However, by further increasing the anodic overpotentials (check anodic branch of polarization curves in Fig. 10) and annihilating the protective oxide film on the as-built surface, Au–Ni coated surfaces showed superior polarization resistance and lower current densities compared to the as-built and polished surface. Higher polarization resistance and lower current densities observed in the polarization curve of the ED Au–Ni coated surface compared to the ELD Au–Ni coated surface can be attributed to the differences in globular size, morphology and uniformity of the agglomerated particles. As shown in Figs. 2 and 4, the globular size of the Au particles observed on the ELD coated surface is relatively smaller than that identified for the ED coated surface. The grain boundaries and crystalline junction points are known to be more electrochemically active than the interior of

the grains as they have reduced atomic packing density due to the mismatches between adjacent crystals [52–56]. Therefore, the more agglomerated particles provide a larger area of mismatching and lead to more active areas on the ELD Au–Ni coated surface compared to ED coated surface.

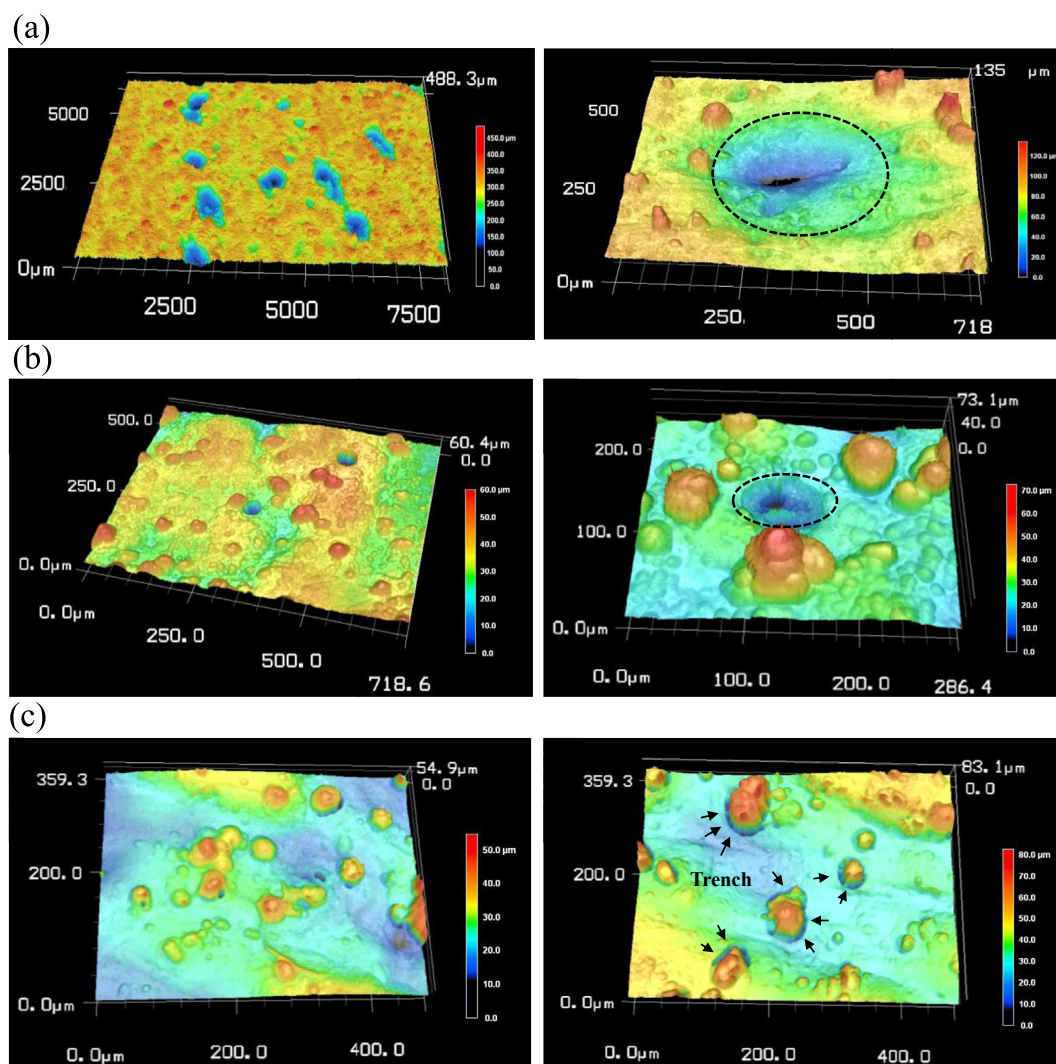
Fig. 11 shows the 3D surface profile of the examining sample after the polarization test. Deep and wide corrosion pits can be seen on the surface of the as-built AM AlSi10Mg sample mostly around incomplete fused powders and porosities. Noticeable localized attack on globular features was also observed on the surface of the ELD Au–Ni coated surface. Nevertheless, the attacks were comparatively minor for the ED Au–Ni coated surface and only trenches were detected around the globular features proving the superior resistance of this surface to anodic dissolution compared to other examining surfaces. As noted previously, the gold element, itself, is a very chemically stable metal, and subtle corrosion attacks observed on the surface of Au–Ni coated surfaces can be attributed to defective areas, such as heterogeneity on the surface, which is attacked by extremely high oxygen evolution during anodic overpotentials.

Fig. 12 shows the electrochemical impedance responses of examining surfaces at OCP after being exposed in 3.5 wt.% NaCl solution for 24 h. Surface roughness and local electrochemical properties changes across the corroding sample renders heterogeneous current distribution along and normal to the surface/solution interface. This alters the ideally polarizable behavior of the surfaces and results in phase angles lower than  $90^\circ$  and the formation of depressed semi-circles in Nyquist plots for capacitive phenomena [57–62]. Thus, all capacitive behavior in this study is interpreted as constant phase elements (CPE).

For as-built and polished AM AlSi10Mg surfaces, the overall EIS spectra show two superimposed capacitive-like behavior. The high-frequency capacitive loop range mainly corresponds to the oxide film/solution interface phenomena (flow of vacancies and ions through oxide or coating). The low-frequency ranges are attributed to the charge transfer and electrical double layer electrochemical response at the interface of metal/solution. In addition formation of scattered points in certain points of medium- and low-frequencies implies coverage of absorbed  $\text{Al}(\text{OH})_3$  on the electrochemically active spots which respond to AC potential stimulations of EIS at certain relaxation time periods [48,63]. The EIS spectra of Au–Ni coated surface yielded only one capacitive-like behavior with the formation of a finite-length diffusion characteristic which can be discerned as a straight line at medium-frequency ranges of the Nyquist plots. As noted before, no oxide film is expected on the Au–Ni coated.

**Table 3** – The anodic and cathodic Tafel slopes ( $\beta_a$  and  $\beta_b$ ), corrosion current density ( $j_{\text{corr}}$ ) as well as corrosion potential ( $E_{\text{corr}}$ ) of the examined samples extracted from the potentiodynamic polarization curves shown in Fig. 10.

Sample	$ \beta_c $ (mV/dec)	$\beta_a$ (mV/dec)	$j_{\text{corr}}$ ( $\mu\text{A}\cdot\text{cm}^{-2}$ )	$E_{\text{corr}}$ (V vs. SCE)
As-built	235.2	197.6	14.4	–0.82
Polished	180.9	15.2	32.1	–0.76
ELD Au–Ni coated AM alloy	200.2	101.8	37.9	–0.74
ED Au–Ni coated AM alloy	207.5	105.1	34.6	–0.75



**Fig. 11** – Surface morphology after applying potentiodynamic polarization on the AM AlSi10Mg alloy with (a) as-built, (b) electroless and (c) electrodeposited Au–Ni coated surface condition.

Therefore, the EIS responses at these surfaces represent the diffusion and Faradaic impedance paralleled with electrical double layer capacitive behavior at OCP [64,65].

To obtain a better understanding of the electrochemical behavior of examining surfaces, the simplified equivalent circuits, shown in Fig. 13 were fitted to the impedance spectra which are shown by straight lines in Fig. 12. In the equivalent circuits used here,  $R_s$  is the ohmic resistance of the solution.  $R_{\text{film}}$  and  $CPE_{\text{film}}$  are attributed to the ionic resistance and the capacitance of the oxide film, respectively.  $R_{\text{ct}}$  and  $CPE_{\text{dl}}$  correspond to the charge transfer resistance and double-layer capacitance at the active corroding area. And the  $R_i$  and  $L$ , respectively, represent the ionic resistance and inductance of absorbed hydroxide ions on the active spots of corroding AlSi10Mg alloy [63]. For the Au–Ni coated surface,  $CPE_{\text{dl}}$  is the capacitance of double-layer form all over the surface.  $R_{\text{ct}}$  and  $W_s$  are associated to charge transfer resistance and Finite Length Warburg (FLW) diffusion resistance for ions taking place metal/solution interface [66].  $\alpha_{\text{film}}$  and  $\alpha_{\text{dl}}$ , are the CPE exponent of the film and double layer, respectively. These

values ( $0 \leq \alpha \leq 1$ ) show the degree of dispersion of a CPE, where  $\alpha = 1$  indicates a pure capacitor without heterogeneity in polarization across or through the surface [61,62].

The extracted electrical parameters from EIS data using the circuits shown in Fig. 13 are listed in Table 4. Comparing the  $R_f$  values of as-built with polished AlSi10Mg samples, it can be seen the natural oxide film formed on the surface of the AM AlSi10Mg part after manufacturing and exposure to the air, has significantly increased the overall resistance of this alloy to corrosion. Also, the greater  $R_{\text{ct}}$  and  $Q_{\text{dl}}$  for as-built compared to the polished surface shows the formation of a thinner space charge layer and higher polarization resistance of electrochemically active spots [37]. Furthermore, higher values of  $L$  for polished surface compared to as-built surface indicates the formation of an extensive amount of  $\text{Al}(\text{OH})_3$  due to increased oxidation of Al ion. In this study, although the corrosion performance of Au–Ni coated samples cannot be compared with Al matrix using EIS data, overall, the lower impedances of Au–Ni surface at OCP can be attributed to higher ionic conductivity and lower

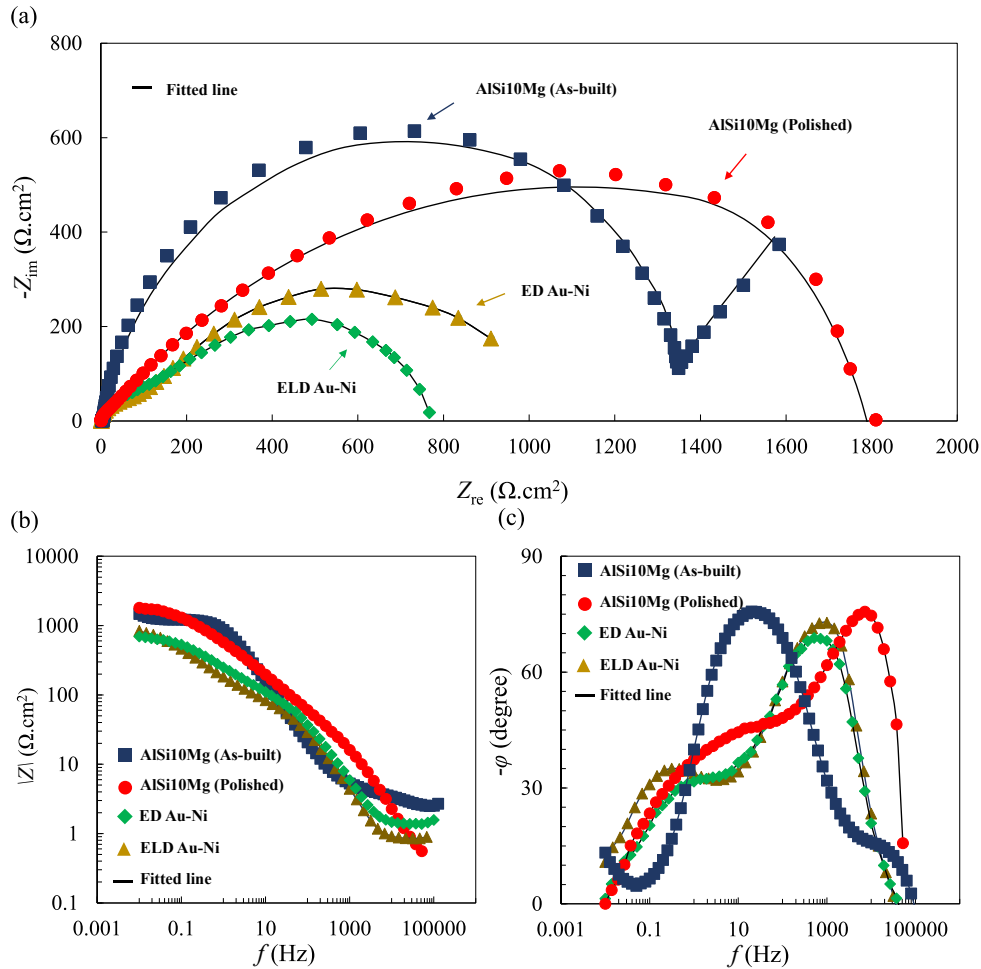


**Fig. 12 – Electrochemical impedance responses of AM AlSi10Mg alloy with as-built, polished and Au-Ni coated surface condition exposed in 3.5 wt.% NaCl solution for 24 h at OCP. (a) Nyquist, (b) Bode and (c) Bode–Phase plots.**

charge transfer resistance of Au in cathodic reaction, which gives superior catalytic properties to these surfaces. Comparing the Warburg diffusion resistance ( $W-R$ ), Warburg time constant ( $W-T$ ) values, it can be seen that ED Au–Ni coated surface is more under the control of ionic diffusion compared to ELD Au–Ni surface which results in higher polarization resistance of ED Au–Ni coated surface [67,68]. In

fact, this result shows the electrochemical reactions, most likely water hydrolysis, occurring on both Au–Ni coated surfaces are under short length diffusion control of ions rather than charge transfer. This kinetic is more pronounced for ED Au–Ni surface.

To this end, the Au–Ni coating using both of the proposed deposition techniques, ED and ELD, is beneficial for enhancing

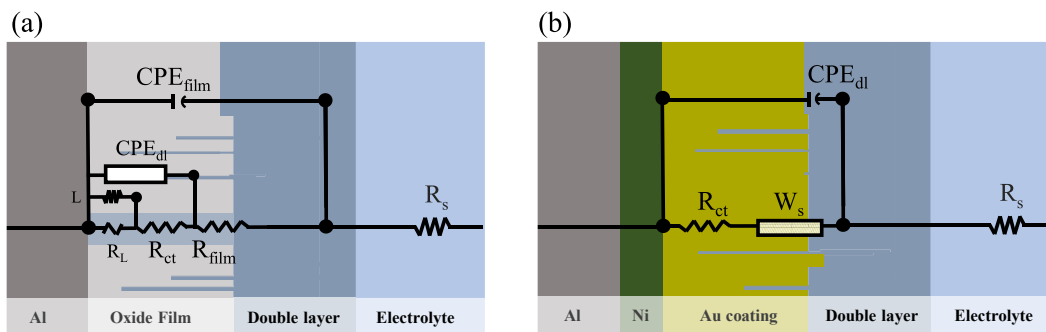


**Fig. 13 – Simplified electrical circuits for (a) as-built and polished surface of AM AlSi10Mg and (b) ED and ELD Au–Ni coatings used for EIS interpretation.**

**Table 4 – Impedance values of examined samples extracted from the Nyquist plots curves shown in Fig. 12.**

Sample	$R_s$ ( $\Omega.cm^2$ )	$R_{film}$ ( $\Omega.cm^2$ )	$Q_{film}$ ( $\mu F.s^{(1-\alpha)}$ . $cm^{-2}$ )	$\alpha_{film}$	$R_{ct}$ ( $\Omega.cm^2$ )	$Q_{dl}$ ( $\mu F.s^{(1-\alpha)}$ . $cm^{-2}$ )	$\alpha_{dl}$	$R_L$ ( $\Omega.cm^2$ )	$L$ ( $H.cm^{-2}$ )	$\chi^2$ ( $\times 10^{-3}$ )
As-built, bare AM alloy	3.2	1420	90.4	0.86	1980	350	0.93	50	22	0.9
Polished, bare AM alloy	3.0	54	4.5	0.88	1795	70.01	0.61	61	150	1.9
	$R_s$ ( $\Omega.cm^2$ )	W-R ( $\Omega.cm^2$ )	W-T (s)	W-P	$R_{ct}$ ( $\Omega.cm^2$ )	$Q_{dl}$ ( $\mu F.s^{(1-\alpha)}$ . $cm^{-2}$ )	$\alpha_{dl}$			$\chi^2$ ( $\times 10^{-3}$ )
ELD Au–Ni coated AM alloy	1.9	799	4.1	0.34	1.1	13.1	0.95	–	–	0.1
ED Au–Ni coated AM alloy	1.2	990	10.1	0.35	1.0	16.1	0.93	–	–	0.09

**Table 5 – Qualitative comparison that highlights the extent of improvement in different properties of AM AlSi10Mg alloy achieved by Au–Ni coating using electrodeposition (ED) and electroless deposition (ELD) techniques.**

Au–Ni coating technique	Micro-hardness	Electrical conductivity	Corrosion resistance
ED	+	+	++
ELD	++	++	+

the surface quality, mechanical response, electrical conductivity and corrosion resistance of L-PBF additively manufactured AlSi10Mg alloy. The current results reveal that the extent of improvement in these properties is different for both techniques. Table 5 highlights the relative enhancement achieved by applying the Au–Ni coating by ED and ELD techniques. Based on the current investigations, a couple of differences are identified to be the parameters that control the extent of improvement in the properties resulting from ED and ELD techniques, as discussed. These differences are the presence of P and graphite in the deposited Au layer by ED and the difference in the size of agglomerated Au particles. Accordingly, this study provides a pathway to decide which coating technique (here ED or ELD) should be followed in order to achieve a set of desired functional properties. Obviously, the ELD technique gives better surface mechanical durability and electrical conductivity, while the ED technique shows better performance when corrosion resistance is of prime importance.

#### 4. Conclusions

Two different Au–Ni coating techniques, namely, electrodeposition (ED) and electroless deposition (ELD) were applied on the additively manufactured AlSi10Mg alloy to enhance its mechanical, electrical and corrosion properties. The most relevant results of the present work can be briefly summarized as follows:

- Both of the ED and ELD techniques are beneficial to completely seal and fill the surface pores and cracks observed in the as-built state, while the surface roughness

is still relatively high due to the presence of Au agglomerated particles.

- The indentation hardness values of the Au layer developed by both ED and ELD techniques show higher values than that of the as-built AM AlSi10Mg alloy. However, the indentation hardness of the deposited Au layer by ELD exhibits better performance than its counterpart developed by ED.
- The measured electrical resistivity values of Au–Ni coatings by both ED and ELD techniques indicate a significant enhancement in the electrical conductivity of AM AlSi10Mg alloy compared with the as-built state. The presence of phosphorous in the Au layer developed by ED seems to increase the electrical resistivity.
- Within 24 h exposure in 3.5 wt.% NaCl aqueous solution, the as-built surface of the additively manufactured AlSi10Mg alloy showed a superior corrosion performance compared to the polished and Au–Ni coated surface conditions. This behavior originates from the presence of air-formed oxide film on the surface of the as-built sample. However, this surface showed high susceptibility to pitting corrosion in anodic potential ranges.
- Both Au–Ni coated samples by means of electroless and electrodeposition showed a superior polarization resistance in anodic polarization ranges compared to the as-built and polished AM AlSi10Mg alloy.

#### Declaration of Competing Interest

The authors declare that they have no known competing financial interests or personal relationships that could have appeared to influence the work reported in this paper.

#### Acknowledgement

The authors would like to acknowledge the financial support received from the Council of Oulu Region, City of Nivala, Nivala Industrial Park Ltd., NIHAK Nivala-Haapajärvi region registered association and the European Union (European Regional Development Fund) for the “Hybridi” and “M3D” projects. We also would like to express our gratitude to Eforit

Oy, Sipoo, Finland for conducting the industrial gold-nickel coatings.

## REFERENCES

- [1] Leal R, Barreiros FM, Alves L, Romeiro F, Vasco JC, Santos M, et al. Additive manufacturing tooling for the automotive industry. *Int J Adv Manuf Technol* 2017;92:1671–6. <https://doi.org/10.1007/s00170-017-0239-8>.
- [2] Agrawal R, Vinodh S. Life cycle assessment of an additive manufactured automotive component. In: Shunmugam MS, Kanthababu M, editors. *Advances in additive manufacturing and joining*. Singapore: Springer Singapore; 2020. p. 219–28.
- [3] Attar H, Ehtemam-Haghighi S, Soro N, Kent D, Dargusch MS. Additive manufacturing of low-cost porous titanium-based composites for biomedical applications: advantages, challenges and opinion for future development. *J Alloys Compd* 2020;827:154263. <https://doi.org/10.1016/j.jallcom.2020.154263>.
- [4] Gebhardt A, Schmidt F-M, Hötter J-S, Sokalla W, Sokalla P. Additive manufacturing by selective laser melting the realizer desktop machine and its application for the dental industry. *Phys Procedia* 2010;5:543–9. <https://doi.org/10.1016/j.phpro.2010.08.082>.
- [5] Uriondo A, Esperon-Miguez M, Perinpanayagam S. The present and future of additive manufacturing in the aerospace sector: a review of important aspects. In: *Proceedings of the institution of mechanical engineers, Part G: journal of aerospace engineering*, vol. 229; 2015. p. 2132–47. <https://doi.org/10.1177/0954410014568797>.
- [6] Froes F. *Additive manufacturing for the aerospace industry*. Amsterdam, Netherlands: Elsevier; 2019.
- [7] Aboulkhair NT, Maskery I, Tuck C, Ashcroft I, Everitt NM. Improving the fatigue behaviour of a selectively laser melted aluminium alloy: influence of heat treatment and surface quality. *Mater Des* 2016;104:174–82. <https://doi.org/10.1016/j.matdes.2016.05.041>.
- [8] Rautio T, Mäkikangas J, Mustakangas A, Mäntyjärvi K. Disk laser assisted surface heat treatments of alsi10mg parts produced by selective laser melting (slm). *Procedia Manuf* 2019;36:95–100. <https://doi.org/10.1016/j.promfg.2019.08.014>.
- [9] Beretta S, Romano S. A comparison of fatigue strength sensitivity to defects for materials manufactured by AM or traditional processes. *Int J Fatig* 2017;94:178–91. <https://doi.org/10.1016/j.ijfatigue.2016.06.020>.
- [10] Yadollahi A, Shamsaei N. Additive manufacturing of fatigue resistant materials: challenges and opportunities. *Int J Fatig* 2017;98:14–31. <https://doi.org/10.1016/j.ijfatigue.2017.01.001>.
- [11] Divya V, Muñoz-Moreno R, Messé O, Barnard J, Baker S, Illston T, et al. Microstructure of selective laser melted CM247lc nickel based superalloy and its evolution through heat treatment. *Mater Char* 2016;114:62–74. <https://doi.org/10.1016/j.matchar.2016.02.004>.
- [12] Xiao D, Yang Y, Su X, Wang Di, Sun J. An integrated approach of topology optimized design and selective laser melting process for titanium implants materials. *Bio Med Mater Eng* 2013;23:433–45.
- [13] Zhang Duyao, Dong Qiu, Gibson Mark A, Zheng Yufeng, Fraser Hamish L, StJohn David H, et al. Additive manufacturing of ultrafine-grained high-strength titanium alloys. *Nature* 2019;576:91–5.
- [14] Clare AT, Chalker PR, Davies S, Sutcliffe CJ, Tsopanos S. Selective laser melting of high aspect ratio 3D nickel–titanium structures two way trained for MEMS applications. *Int J Mech Mater Des* 2008;4:181–7.
- [15] Song H, McGaughey T, Sadek A, Zhang W. Effect of structural support on microstructure of nickel base superalloy fabricated by laser-powder bed fusion additive manufacturing. *Additive Manufacturing* 2019;26:30–40.
- [16] Badrossamay M, Childs THC. Further studies in selective laser melting of stainless and tool steel powders. *Int J Mach Tool Manuf* 2007;47:779–84.
- [17] Allam T, Pradeep KG, Köhnen P, Marshal A, Schleifenbaum JH, Haase C. Tailoring the nanostructure of laser powder bed fusion additively manufactured maraging steel. *Additive Manufacturing* 2020;36:101561.
- [18] Buchbinder D, Schleifenbaum H, Heidrich S, Meiners W, Bültmann J. High power selective laser melting (HP SLM) of aluminum parts. *Phys Procedia* 2011;12:271–8.
- [19] Aboulkhair NT, Simonelli M, Parry L, Ashcroft I, Tuck C, Hague R. 3D printing of Aluminium alloys: additive Manufacturing of Aluminium alloys using selective laser melting. *Prog Mater Sci* 2019;106:100578.
- [20] Buchbinder D, Schleifenbaum H, Heidrich S, Meiners W, Bültmann J. High power selective laser melting (HP SLM) of aluminum parts. *Phys Procedia* 2011;12:271–8. <https://doi.org/10.1016/j.phpro.2011.03.035>.
- [21] Read N, Wang W, Essa K, Attallah MM. Selective laser melting of AlSi10Mg alloy: process optimisation and mechanical properties development. *Mater Des* 2015;65:417–24. <https://doi.org/10.1016/j.matdes.2014.09.044>.
- [22] Mäkikangas J, Rautio T, Mustakangas A, Mäntyjärvi K. Laser welding of alsi10mg aluminium-based alloy produced by selective laser melting (slm). *Procedia Manuf* 2019;36:88–94. <https://doi.org/10.1016/j.promfg.2019.08.013>.
- [23] Uzan NE, Shneck R, Yeheskel O, Frage N. Fatigue of AlSi10mg specimens fabricated by additive manufacturing selective laser melting (AM-SLM). *Mater Sci Eng, A* 2017;704:229–37. <https://doi.org/10.1016/j.msea.2017.08.027>.
- [24] Brandl E, Heckenberger U, Holzinger V, Buchbinder D. Additive manufactured AlSi10mg samples using selective laser melting (SLM): microstructure, high cycle fatigue, and fracture behavior. *Mater Des* 2012;34:159–69. <https://doi.org/10.1016/j.matdes.2011.07.067>.
- [25] Tang M, Pistorius PC. Oxides, porosity and fatigue performance of AlSi10mg parts produced by selective laser melting. *Int J Fatig* 2017;94:192–201. <https://doi.org/10.1016/j.ijfatigue.2016.06.002>.
- [26] Kempen K, Thijs L, Humbeeck JV, Kruth J-P. Processing AlSi10mg by selective laser melting: parameter optimisation and material characterisation. *Mater Sci Technol* 2014;31:917–23. <https://doi.org/10.1179/1743284714y.0000000702>.
- [27] Read N, Wang W, Essa K, Attallah MM. Selective laser melting of AlSi10Mg alloy: process optimisation and mechanical properties development. *Mater Des (1980–2015)* 2015;65:417–24.
- [28] Thijs L, Kempen K, Kruth J-P, Humbeeck JV. Fine-structured aluminium products with controllable texture by selective laser melting of pre-alloyed AlSi10mg powder. *Acta Mater* 2013;61:1809–19. <https://doi.org/10.1016/j.actamat.2012.11.052>.
- [29] Wu J, Wang XQ, Wang W, Attallah MM, Loretto MH. Microstructure and strength of selectively laser melted AlSi10Mg. *Acta Mater* 2016;117:311–20.
- [30] Tang M, Pistorius PC, Narra S, Beuth JL. Rapid solidification: selective laser melting of AlSi10Mg. *JOM* 2016;68:960–6.
- [31] Silbernagel C, Ashcroft I, Dickens P, Galea M. Electrical resistivity of additively manufactured AlSi10mg for use in electric motors. *Additive Manufacturing* 2018;21:395–403. <https://doi.org/10.1016/j.addma.2018.03.027>.
- [32] Rautio T, Hamada A, Kumpula J, Järvenpää A, Allam T. Enhancement of electrical conductivity and corrosion

- resistance by silver shell-copper core coating of additively manufactured AlSi10Mg alloy. *Surf Coating Technol* 2020;403:126426. <https://doi.org/10.1016/j.surfcoat.2020.126426>.
- [33] Inberg A, Ashkenazi D, Kimmel G, Shacham-Diamand Y, Stern A. Gold plating of AlSi10Mg parts produced by a laser powder-bed fusion additive manufacturing technique. *Progress in Additive Manufacturing* 2020;5:395–404. <https://doi.org/10.1007/s40964-020-00134-6>.
- [34] Ashkenazi D, Inberg A, Shacham-Diamand Y, Stern A. Gold, silver, and electrum electrodeless plating on additively manufactured laser powder-bed fusion AlSi10Mg parts: a review. *Coatings* 2021;11:422. <https://doi.org/10.3390/coatings11040422>.
- [35] Inberg A, Ashkenazi D, Kimmel G, Shacham-Diamand Y, Stern A. Gold–silver electrodeless plating on laser powder-bed fusion additively printed AlSi10Mg parts. *Metals* 2020;10:557. <https://doi.org/10.3390/met10050557>.
- [36] Pezzato L, Dabalà M, Gross S, Brunelli K. Effect of microstructure and porosity of AlSi10Mg alloy produced by selective laser melting on the corrosion properties of plasma electrolytic oxidation coatings. *Surf Coating Technol* 2020;404:126477. <https://doi.org/10.1016/j.surfcoat.2020.126477>.
- [37] Rafieezad M, Mohammadi M, Gerlich A, Nasiri A. Enhancing the corrosion properties of additively manufactured AlSi10Mg using friction stir processing. *Corrosion Sci* 2021;178:109073. <https://doi.org/10.1016/j.corsci.2020.109073>.
- [38] Ravi R, Paul A. Diffusion mechanism in the gold-copper system. *J Mater Sci Mater Electron* 2012;23:2152–6. <https://doi.org/10.1007/s10854-012-0729-2>.
- [39] Mower TM, Long MJ. Mechanical behavior of additive manufactured, powder-bed laser-fused materials. *Mater Sci Eng, A* 2016;651:198–213. <https://doi.org/10.1016/j.msea.2015.10.068>.
- [40] Aboulkhair NT, Everitt NM, Ashcroft I, Tuck C. Reducing porosity in AlSi10Mg parts processed by selective laser melting. *Addit. Manuf.* 2014;1–4:77–86. <https://doi.org/10.1016/j.addma.2014.08.001>.
- [41] Weingarten C, Buchbinder D, Pirch N, Meiners W, Wissenbach K, Poprawe R. Formation and reduction of hydrogen porosity during selective laser melting of AlSi10Mg. *J Mater Process Technol* 2015;221:112–20. <https://doi.org/10.1016/j.jmatprotec.2015.02.013>.
- [42] Martin JH, Yahata BD, Hundley JM, Mayer JA, Schaedler TA, Pollock TM. 3D printing of high-strength aluminium alloys. *Nature* 2017;549:365–9. <https://doi.org/10.1038/nature23894>.
- [43] Yang KV, Rometsch P, Jarvis T, Rao J, Cao S, Davies C, et al. Porosity formation mechanisms and fatigue response in Al-Si-Mg alloys made by selective laser melting. *Mater Sci Eng, A* 2018;712:166–74. <https://doi.org/10.1016/j.msea.2017.11.078>.
- [44] Coble AJ, Mason TJ, Alarjah M, Ashayer R, Mannan SH. The effect of ultrasound on the gold plating of silica nanoparticles for use in composite solders. *Ultrason Sonochem* 2011;18:37–41. <https://doi.org/10.1016/j.ultsonch.2010.04.010>.
- [45] Gui MC, Jia J, Li QC, Guo WQ. Influences of trace additions of strontium and phosphorus on electrical resistivity and viscosity of liquid Al-Si alloys. *Trans Nonferrous Metals Soc China* 1997;7:67–71.
- [46] Ebrahim-Ghajari M, Allahkaram SR, Mahdavi S. Corrosion behaviour of electrodeposited nanocrystalline co and co/ZrO<sub>2</sub>nanocomposite coatings. *Surf Eng* 2014;31:251–7. <https://doi.org/10.1179/1743294414y.0000000355>.
- [47] Torbati-Sarraf H, Stannard TJ, La Plante EC, Sant GN, Chawla N. Direct observations of microstructure-resolved corrosion initiation in AA7075-T651 at the nanoscale using vertical scanning interferometry (VSI). *Mater Char* 2020;161:110166.
- [48] Torbati-Sarraf H, Torbati-Sarraf SA, Chawla N, Poursae A. A comparative study of corrosion behavior of an additively manufactured Al-6061 RAM2 with extruded Al-6061 T6. *Corrosion Sci* 2020;174:108838. <https://doi.org/10.1016/j.corsci.2020.108838>.
- [49] Finkelstein NP, Hancock RD. A new approach to the chemistry of gold. *Gold Bull* 1974;7:72–7. <https://doi.org/10.1007/BF03215041>.
- [50] Cameron D, Holliday R, Thompson D. Gold's future role in fuel cell systems. *J Power Sources* 2003;118:298–303. [https://doi.org/10.1016/S0378-7753\(03\)00074-0](https://doi.org/10.1016/S0378-7753(03)00074-0).
- [51] Palaniappa M, Jayalakshmi M, Balasubramanian K. Effect of zincation/sonication on electroplated gold deposited on aluminum substrate. *J Mater Eng Perform* 2011;20:1028–35. <https://doi.org/10.1007/s11665-010-9715-0>.
- [52] Ding L, Torbati-Sarraf H, Poursae A. The influence of the sandblasting as a surface mechanical attrition treatment on the electrochemical behavior of carbon steel in different pH solutions. *Surf Coating Technol* 2018;352:112–9. <https://doi.org/10.1016/j.surfcoat.2018.08.013>.
- [53] Ralston KD, Birbilis N. Effect of grain size on corrosion: a review. *Corrosion* 2010;66. <https://doi.org/10.5006/1.3462912.075005-075005-13>.
- [54] Ralston K, Birbilis N, Davies C. Revealing the relationship between grain size and corrosion rate of metals. *Scripta Mater* 2010;63:1201–4. <https://doi.org/10.1016/j.scriptamat.2010.08.035>.
- [55] Wagner M. Structure and thermodynamic properties of nanocrystalline metals. *Phys Rev B* 1992;45:635–9. <https://doi.org/10.1103/physrevb.45.635>.
- [56] Torbati-Sarraf H, Torbati-Sarraf SA, Poursae A, Langdon TG. Electrochemical behavior of a magnesium ZK60 alloy processed by high-pressure torsion. *Corrosion Sci* 2019;154:90–100. <https://doi.org/10.1016/j.corsci.2019.04.006>.
- [57] Torbati-Sarraf H, Ghamarian I, Poorganji B, Torbati-Sarraf S. An investigation on the role of crystallographic texture on anisotropic electrochemical behavior of a commercially pure nickel manufactured by laser powder bed fusion (L-PBF) additive manufacturing. *Electrochim Acta* 2020;354:136694. <https://doi.org/10.1016/j.electacta.2020.136694>.
- [58] Córdoba-Torres P. Characterization of frequency dispersion in the impedance response of a distributed model from the mathematical properties of the distribution function of relaxation times. *Electrochim Acta* 2015;180:591–603. <https://doi.org/10.1016/j.electacta.2015.08.140>.
- [59] Cooper SJ, Bertei A, Finegan DP, Brandon NP. Simulated impedance of diffusion in porous media. *Electrochim Acta* 2017;251:681–9. <https://doi.org/10.1016/j.electacta.2017.07.152>.
- [60] Córdoba-Torres P, Mesquita TJ, Nogueira RP. Relationship between the origin of constant-phase element behavior in electrochemical impedance spectroscopy and electrode surface structure. *J Phys Chem C* 2015;119:4136–47. <https://doi.org/10.1021/jp512063f>.
- [61] Córdoba-Torres P. Relationship between constant-phase element (CPE) parameters and physical properties of films with a distributed resistivity. *Electrochim Acta* 2017;225:592–604. <https://doi.org/10.1016/j.electacta.2016.12.087>.
- [62] Alexander CL, Tribollet B, Vivier V, Orazem ME. Contribution of surface distributions to constant-phase-element (CPE) behavior: 3. adsorbed intermediates. *Electrochim Acta* 2017;251:99–108. <https://doi.org/10.1016/j.electacta.2017.08.081>.
- [63] Keddad M, Kuntz C, Takenouti H, Schustert D, Zuili D. Exfoliation corrosion of aluminium alloys examined by

- electrode impedance. *Electrochim Acta* 1997;42:87–97. [https://doi.org/10.1016/0013-4686\(96\)00170-3](https://doi.org/10.1016/0013-4686(96)00170-3).
- [64] Costa JS, Prestat M, Tribollet B, Lescop B, Rioual S, Holzer L, et al. Impedance spectroscopy analysis of structural defects in sputtered ZnO films. *Chemelectrochem* 2020;7:2055–64. <https://doi.org/10.1002/celec.202000087>.
- [65] Keiser H, Beccu K, Gutjahr M. Estimation of the pore structure of porous electrodes from impedance measurements. *Electrochim Acta* 1976;21:539–43. [https://doi.org/10.1016/0013-4686\(76\)85147-x](https://doi.org/10.1016/0013-4686(76)85147-x).
- [66] Xiao Z, Li Z, Zhu A, Zhao Y, Chen J, Zhu Y. Surface characterization and corrosion behavior of a novel gold-imitation copper alloy with high tarnish resistance in salt spray environment. *Corrosion Sci* 2013;76:42–51. <https://doi.org/10.1016/j.corsci.2013.05.026>.
- [67] Sah SP. Corrosion of 304 stainless steel in carbonates melt— a state of enhanced dissolution of corrosion products. *Corrosion Sci* 2020;169:108535. <https://doi.org/10.1016/j.corsci.2020.108535>.
- [68] Pajkossy T. Impedance spectroscopy at interfaces of metals and aqueous solutions — surface roughness, CPE and related issues. *Solid State Ionics* 2005;176:1997–2003. <https://doi.org/10.1016/j.ssi.2004.06.023>.